2nd Advanced Optical Metrology Compendium

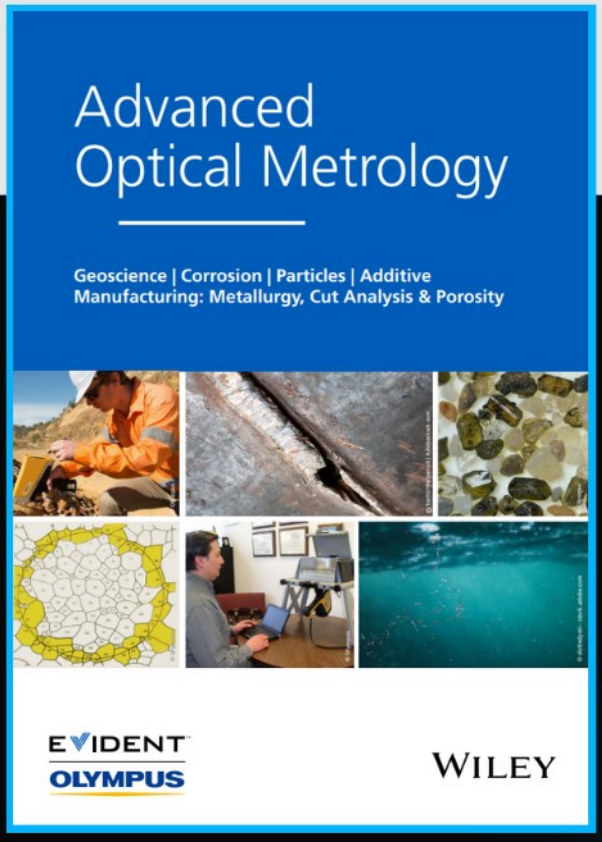

The latest eBook from Advanced Optical Metrology. Download for free.

This compendium includes a collection of optical metrology papers, a repository of teaching materials, and instructions on how to publish scientific achievements.

With the aim of improving communication between fundamental research and industrial applications in the field of optical metrology we have collected and organized existing information and made it more accessible and useful for researchers and practitioners.

EVIDENT
OLYMPUS

WILEY

ADVANCED FUNCTIONAL MATERIALS
www.afm-journal.de

A Programmable Electrochemical Y-Shaped DNA Scaffold Sensor for the Single-Step Detection of Antibodies and Proteins in Untreated Biological Fluids

*Andrea Idili, Andrea Bonini, Claudio Parolo, Ruslán Alvarez-Diduk, Fabio Di Francesco, and Arben Merkoçi**

Proteins and antibodies are key biomarkers for diagnosing and monitoring specific medical conditions. Currently, gold standard techniques used for their quantification require laborious multi-step procedures, involving high costs and slow response times. It is possible to overcome these limitations by exploiting the chemistry and programmability of DNA to design a reagentless electrochemical sensing platform. Specifically, three DNA single strands are engineered that can self-assemble into a Y-shaped DNA nanostructure that resembles one of the IgGs. In order to convert this DNA nanostructure into a responsive DNA-scaffold bioreceptor, it is modified including two recognition elements, two redox tag molecules, and a thiol group. In the absence of the target, the scaffold receptor can efficiently collide with the electrode surface and generate a strong electrochemical signal. The presence of the target induces its bivalent binding, which produces steric hindrance interactions that limit the receptor's collisional activity. In its bound state, the redox tags can therefore approach the surface at a slower rate, leading to a signal decrease that is quantitatively related to the target concentration. The Y-shape DNA scaffold sensor can detect nanomolar concentrations of antibodies and proteins in <15 min with a single-step procedure directly in untreated biological fluids.

1. Introduction

The development of a sensing platform capable of supporting the single-step detection of clinically relevant antibodies and proteins would strongly impact the current diagnostic approaches through high-frequency tests.[1,2] This, for example, would enable mass serological screening directly from untreated clinical samples, thereby reducing the time lag between the diagnosis and the treatment (e.g., from infective to autoimmune diseases),[3,4] enabling easier global health monitoring and surveillance (i.e., monitoring vaccination statuses).[5–7] This new diagnostic technology needs not only to be rapid (i.e., taking <10 min), quantitative, highly specific, and adaptable to a wide range of diseases, but also to have a high-throughput (i.e., capable of precisely analyzing hundreds of samples in a short time) and be easy to use so that even non-trained personnel would be able to perform the tests properly.[8] In contrast, current clinical approaches do not fulfill all these analytical requirements. For example, laboratory-based techniques such as the enzyme-linked immunosorbent assay (ELISA) and Western blot assay require reagent-intensive and multi-step processes (e.g., washings, incubations, and sample treatments).[9,10] On the other hand, point-of-care devices, such as lateral flow assays (LFA), can perform the naked eye detection of specific biomarkers in <15 min, however, they show low sensitivity and specificity, as well as the inability to precisely quantify the target.[3,11,12] Consequently, a sensing technology that synergically combines the high sensitivity and specificity of laboratory-based techniques with the speed and convenience of

A. Idili, A. Bonini, C. Parolo, R. Alvarez-Diduk, A. Merkoçi
Catalan Institute of Nanoscience and Nanotechnology (ICN2)
campus UAB, Bellaterra, 08193 Barcelona, Spain
E-mail: arben.merkoci@icn2.cat

The ORCID identification number(s) for the author(s) of this article can be found under https://doi.org/10.1002/adfm.202201881.

© 2022 The Authors. Advanced Functional Materials published by Wiley-VCH GmbH. This is an open access article under the terms of the Creative Commons Attribution-NonCommercial-NoDerivs License, which permits use and distribution in any medium, provided the original work is properly cited, the use is non-commercial and no modifications or adaptations are made.

DOI: 10.1002/adfm.202201881

A. Bonini, F. Di Francesco
Department of Chemistry and Industrial Chemistry
University of Pisa
56124 Pisa, Italy

C. Parolo
ISGlobal, Barcelona Centre for International Health Research (CRESIB)
Hospital Clínic (Department of International Health)
Universitat de Barcelona
08036 Barcelona, Spain

A. Merkoçi
CSIC and the Barcelona Institute of Science and Technology (BIST)
08036 Barcelona, Spain

A. Merkoçi
Institució Catalana de Recerca i Estudis Avançats (ICREA)
08010 Barcelona, Spain

Check for updates
16163028, 2022, 37, Downloaded from https://onlinelibrary.wiley.com/doi/10.1002/adfm.202201881 by Universita Degli Studi Di Roma, Wiley Online Library on [25/01/2023]. See the Terms and Conditions (https://onlinelibrary.wiley.com/terms-and-conditions) on Wiley Online Library for rules of use; OA articles are governed by the applicable Creative Commons License

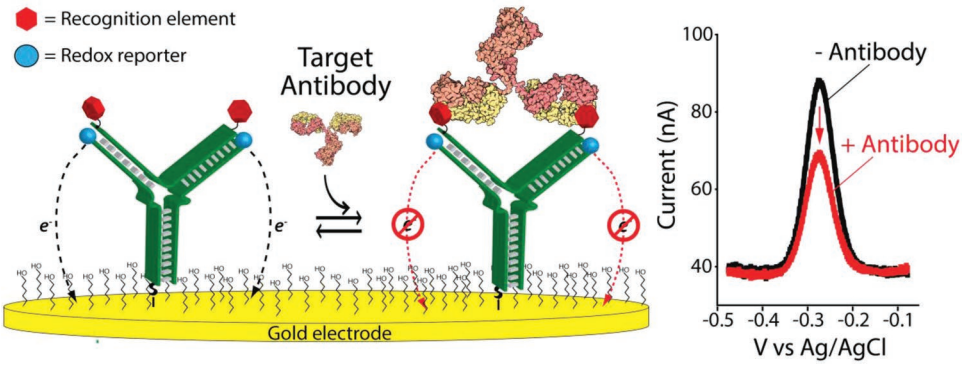

Figure 1. Y-shaped DNA scaffold sensors consists of a nucleic acid "scaffold" nanostructure designed i) to mimic the natural shape of the bivalent immunoglobulin G antibodies and ii) to be bound to a gold surface via a flexible hexanethiol linker. The arms of the scaffold are modified with two recognition molecules and two redox reporters (here methylene blue). (Left) Binding of the target antibody to the recognition elements reduces the frequency with which the redox reporters collide with the electrode surface, resulting in a decrease of the faradic current collected using square wave voltammetry. (Right) Representative square wave voltammograms of the unbound and target-bound scaffold sensor (for the detection of 100×10^{-9} M anti-digoxigenin antibody in 100% serum).

point-of-care testing could have a significant impact on current diagnostics.

New biosensing platforms have been developed over the last two decades to achieve reagentless, single-step detection of antibodies (or proteins) directly in untreated biological fluids.[13–15] These platforms exploit synthetic, redox-labeled nucleic acid molecules as responsive recognition elements that generate electrochemical signals in response to the presence of the selected target.[16–18] For example, biosensors based on DNA aptamers or antigen-tagged DNA probes can fold/unfold in the presence of the biomolecular target (i.e., they undergo a binding-induced conformational change) generating a specific electrochemical signal.[19–21] Besides their elegant design and versatility, their main advantage is that they exhibit higher specificity, since to generate the signal, the bioreceptor has to undergo a binding-induced conformational change; an approach similar to the one observed in natural receptors.[22,23] However, these biosensors are often expensive (due to internal modifications[24] of the DNA sequence), and require a precise thermodynamic characterization to enhance the conformational change on the electrode surface, which directly affects the overall analytical performance of the sensor.[25,26] Sensors based on DNA-scaffold receptors (i.e., double-stranded DNA presenting a recognition element) have been deployed to fully succeed in the detection and monitoring (for many hours) of antibodies and proteins in undiluted samples (e.g., serum, blood, and saliva).[27–32] Their advantages rely on a minimalist design since the signal production depends mostly on the steric hindrance produced by the binding of the antibody or protein to its recognition element that is attached to the DNA scaffold. Despite these sensors being able to detect antibodies, proteins, and even viral particles in a single step, the generation of the signal is strongly affected by the size of the selected recognition element (epitope or antigen).[30–33] Moreover, their design do not take advantage of the structure of natural receptors such as antibodies or multivalent proteins, as any sufficiently large monovalent target that induces adequate steric hindrance can generate a measurable signal.

In this study, we expand the set of DNA scaffold sensing architectures by introducing a novel geometry that takes inspiration from the structure of natural Immunoglobulin G (IgG) antibodies (**Figure 1**). Specifically, we employed as a recognition element a DNA "scaffold" nanostructure rationally designed to assume a Y-shaped structure through the self-assembly of three modified DNA single strands (Figure 1). The arms of the nanostructure are modified with two recognition elements, placed at a distance equal to the two paratopes of human IgGs, and two redox tag molecules (i.e., methylene blue). Thanks to this configuration, the scaffold sensor can bind bivalently to its target inducing stronger steric hindrance interactions and the suppression of the faradic current. At the same time, the use of two methylene blue reporters generates an electrochemical signal strong enough to support the detection of the target directly in biological fluids. Using three different recognition elements (digoxigenin, DNP, and biotin), we showed how our sensing platform is highly programmable and can fully support the rapid, single-step detection of antibodies and proteins directly in undiluted biological matrices (serum and artificial saliva) at nanomolar concentrations.

2. Results and Discussion

2.1. Design

Our strategy to develop a programmable DNA-scaffold sensor for the rapid, single-step detection of antibodies (or proteins) is based on the use of three complementary DNA single strands that have been designed to be assembled in a Y-shaped nanostructure (**Figure 2**). The sequence of each single strand has two "stem" portions (20-base; Figure 2A), separated by a poly(T) linker of five bases, which have been designed to bind their complementary "stem" sequences present in the other two strands (Figure 2A, red, green, and blue domains). To induce binding with the selected target antibody and to adapt it so that it can support an electrochemical platform, we modified the DNA nanostructure with specific functional groups and electroactive tag molecules. More specifically, the first strand (anchoring strand 1, Figure 2A) was modified at 5′-end with a

© 2022 The Authors. Advanced Functional Materials published by Wiley-VCH GmbH

16163028, 2022, 37, Downloaded from https://onlinelibrary.wiley.com/doi/10.1002/adfm.202201881 by Universita Degli Studi Di Roma, Wiley Online Library on [25/01/2023]. See the Terms and Conditions (https://onlinelibrary.wiley.com/terms-and-conditions) on Wiley Online Library for rules of use; OA articles are governed by the applicable Creative Commons License

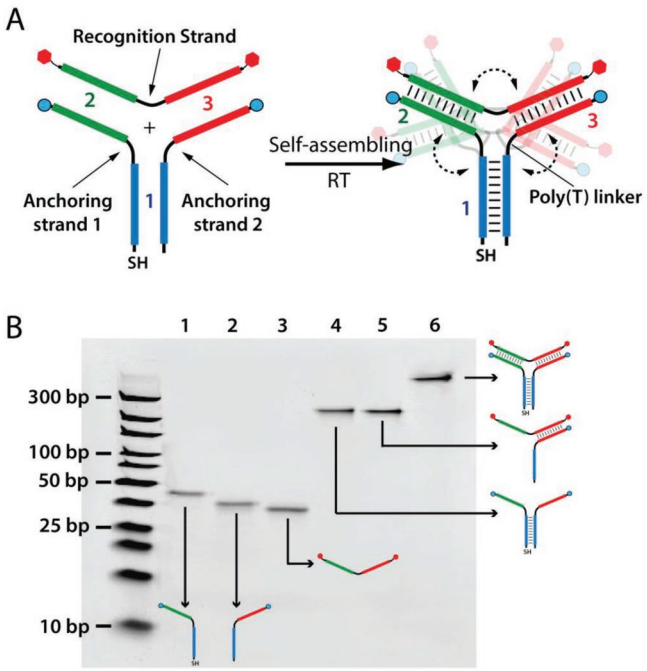

Figure 2. A) The Y-shaped scaffold structure is made up of three functionalized DNA single strands: the "anchoring strand 1" modified at its two ends with a thiol group, and a methylene blue molecule; the "recognition strand" modified with two recognition molecules on its extremities; and the "anchoring strand 2" that holds only a methylene blue molecule. Their self-assembly (driven by Watson-Crick-Franklin interactions) induces the formation of three duplex "stem" portions (length of 20 base pairs each; red, green, and blue domains), interconnected by three linkers composed of five thymines, resulting in a Y-shaped nanostructure. The single strand core formed by the poly(T) linkers ensures that the two recognition arms have sufficient flexibility and conformational variability,[41,42] thus mimicking findings observed with IgG antibodies, where the two paratopes can finely modulate their distance to improve the bivalent binding with their target.[43–46,53] B) The non-denaturing polyacrylamide gel electrophoresis (PAGE) experiment confirms the formation of the scaffold nanostructure. Lanes 1, 2, and 3 show individual bands of the DNA single strand which, as expected, display the highest mobility, and correspond to the "anchoring strand 1", "anchoring strand 2", and "recognition strand", respectively. Lanes 4 and 5 show individual bands corresponding to the hybridization of the two anchoring strands and the hybridization of "anchoring strand 2" and the "recognition strand", respectively. Finally, lane 6 shows the band corresponding to the efficient formation of the full Y-shaped DNA scaffold, which, as expected, displays the lowest mobility in the gel.

thiol group (to anchor the nanostructure to the gold electrode surface) and at the 3′-end with the methylene blue. Both ends of the second strand (recognition strand, Figure 2A) were modified with two equal recognition molecules. Last, only the 5′-end of the third strand (anchoring strand 2, Figure 2A) was modified with the methylene blue. Once in solution, the three functionalized strands hybridize to form a Y-shaped DNA nanostructure where the "stem" portion 1 (blue domain) is connected to the gold electrode surface, while both arms (stem portions 2 and 3, red and green domains) are oriented toward the bulk solution sharing the same methylene blue and recognition molecules.

The design of our scaffold sensor takes advantage of the natural shape of IgGs and their bivalent interactions with their molecular targets.[34,35] Specifically, we exploited the programmability of DNA as nanomaterial[36–38] to engineer a Y-shaped nanostructure . At the same time, we exploited the random coil conformation of poly(T) linkers[39,40] to introduce high flexibility to the two responsive arms, and more in general, to the overall structure.[41,42] This configuration was designed to mimic the high conformational variability and dynamics observed in natural IgGs, which are crucial for their outstanding binding activity.[43–46] We therefore believe that this geometry should guarantee the bivalent binding between one single antibody and one Y-shaped DNA scaffold. We thus validated the design of our scaffold receptor using the nucleic acid folding predictor NUPACK.[47] This software confirmed the correct design and assembly of the three strands. As expected, the three double strand "stem" portions were found to be interconnected by poly(T) linkers forming a Y-shape structure (Figure S1, Supporting Information). After this simulative test, we experimentally demonstrated the assembly of the Y-shaped DNA structure (Figure 2B) using non-denaturing polyacrylamide gel electrophoresis (PAGE). PAGE is a valid and reliable method for characterizing the formation and yield of DNA nanostructure assemblies.[48–50] This experiment clearly showed that mixing the three modified oligos in the same solution using a 1:1:1 molar ratio, at room temperature leads to the formation of a single band with the lowest mobility corresponding to the assembled scaffold receptor (Figure 2B, lane 6). In contrast, the single strands (Figure 2C, lanes 1,2, and 3) and the two self-complementary duplex dimers (Figure 2C, lanes 4 and 5) showed a higher mobility due to their lower weights and smaller size. These data are in agreement with previous studies involving the use of similar DNA-based structures based on a three-way junction.[51,52] After demonstrating the correct assembly, we set out the immobilization and characterization of our Y-shaped receptor on the electrochemical platform.

2.2. Sensing Mechanism

Y-shaped DNA-scaffold sensors can promptly detect the presence of the selected target antibody when interrogated using square-wave voltammetry (SWV) (Figures S2 and S3, Supporting Information). We first demonstrated how the signal-transduction mechanism relies on the collisional activity of the Y-shaped DNA scaffold receptor with the gold electrode surface. To achieve this, we selected the detection of anti-digoxigenin antibodies as a testbed (**Figure 3**A, left). We decided to use the steroid digoxigenin as a recognition element because this system has been previously exploited to characterize other DNA nanotechnology-based serological sensors,[24,33,54,55] due to the ease of synthesizing digoxigenin-modified DNA molecules. In the absence of the target, the modified Y-shaped scaffold receptor is free to collide with the electrode surface (Figure 1, left) and can produce a large current at the redox potential expected for methylene blue (Figure 1, right). The presence of the antibody decreases this faradic current because the bulky antibody-scaffold receptor complex limits the movements that allow the redox reporters to approach the electrode surface. To demonstrate this collisional mechanism and how binding-induced steric hindrance interactions drive the signal-transduction mechanism of the sensor, we characterized how the signal gain

© 2022 The Authors. Advanced Functional Materials published by Wiley-VCH GmbH

16163028, 2022, 37, Downloaded from https://onlinelibrary.wiley.com/doi/10.1002/adfm.202201881 by Universita Degli Studi Di Roma, Wiley Online Library on [25/01/2023]. See the Terms and Conditions (https://onlinelibrary.wiley.com/terms-and-conditions) on Wiley Online Library for rules of use; OA articles are governed by the applicable Creative Commons License

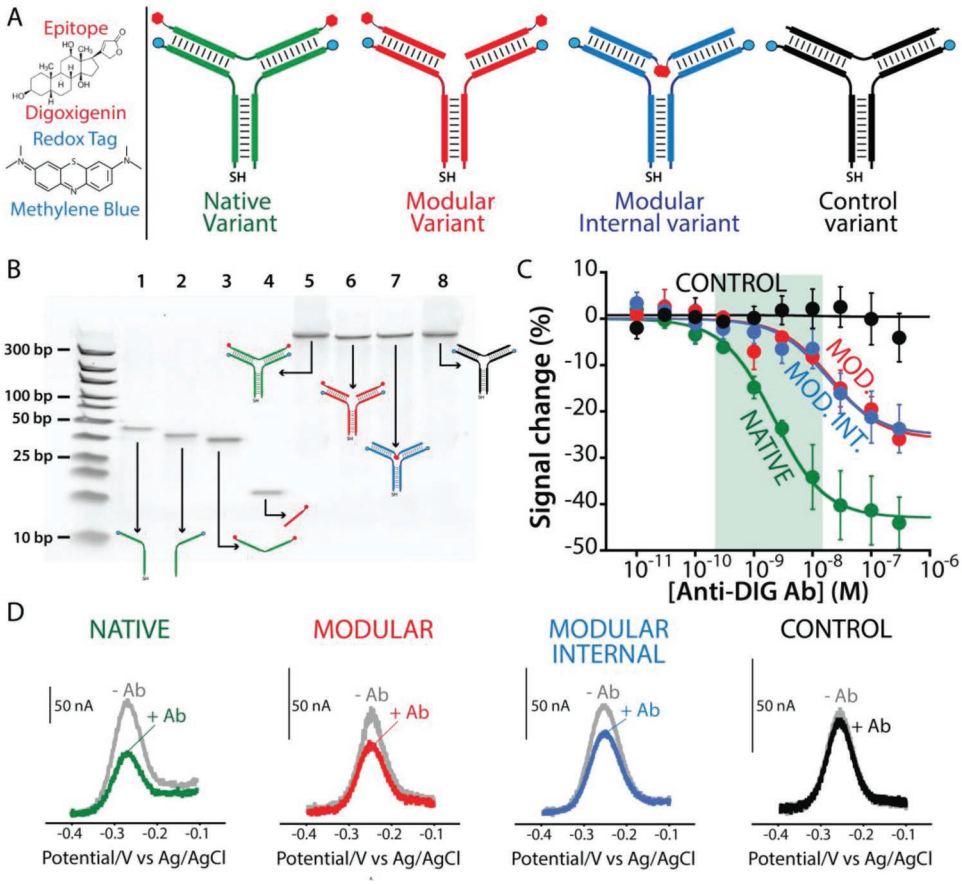

Figure 3. A) To characterize our new sensing platform, as model system, we detected anti-Dig antibodies using two molecules of digoxigenin (Dig) as recognition elements. We designed four different DNA-scaffold variants introducing in their structures different degrees of flexibility (removing one poly(T) linker from the core; red variant) and positioning the recognition molecules (removing or moving them in the inner part of the structure; black and blue variant). B) Native PAGE gel confirms the full assembly of the scaffold variants. C) The electrochemical detection of anti-digoxigenin antibodies using the four different variants indicates that the one producing the most sensitive response with the biggest signal change is the native variant (green line). The error bars reflect standard deviations derived using at least three independently fabricated sensors. D) Representative square wave voltammograms collected in the absence (gray) and in the presence of the antibody target (colored), for the different variants (for the detection of 100×10^{-9} M anti-digoxigenin antibody in buffer).

(i.e., the relative change in signal upon the addition of the saturating target) is affected by 1) the frequency of the interrogating SWV potential pulse; and 2) the density with which the scaffold receptors are packed on the electrode surface.

Previous studies have indicated that the signal gain of DNA-scaffold sensors exhibits a slight dependence on the SWV frequency applied during the measurements.[56,57] To better understand this observation, their sensing mechanism needs to be taken into account. As described above, the binding with an antibody induces sufficient steric hindrance to slow down the collisional dynamics of the redox tags with the electrode (without altering the conformational state of the scaffold receptor). The binding event does not change the electron transfer rate of the methylene blue molecules but only reduces the efficiency of the process. Therefore changes in the frequency of the SWV slightly impact the magnitude and the sign (i.e., producing either signal-on or signal-off behavior) of the signal change observed.[56,57] Specifically, the sensors display a signal-off behavior for almost all the range of SWV frequencies (from 1 to 1000 Hz) and a comparable signal gain.[56,57] On the other hand, the amount of receptor chemisorbed on the surface strongly affects the magnitude of the sensor's signal gain.[28,33,58] More specifically, at high densities, receptors are highly packed on the electrode surface and, as they are in close contact with each other, they can limit their collisional movement by decreasing the overall signal change in presence of the target. At low densities, the receptors are far from each other, and are free to approach the surface resulting in a higher signal change in the presence of the antibody target.

To demonstrate the collisional mechanism of the Y-shaped DNA scaffold, we tested our sensors in the presence of saturating (100×10^{-9} M) anti-DIG antibodies and characterized the sensor's response over SWV frequencies ranging from 5 to 1000 Hz. We also used different DNA-probe densities by changing the concentration of scaffold receptors used during the surface functionalization step (Figure S2, Supporting Information). As expected, all the scaffold sensors produced a signal-off behavior and the magnitude of their signal gain was inversely related to the density of the DNA probe on the electrode. The largest signal gain (≈43%) and highest affinity

© 2022 The Authors. Advanced Functional Materials published by Wiley-VCH GmbH

16163028, 2022, 37, Downloaded from https://onlinelibrary.wiley.com/doi/10.1002/adfm.202201881 by Universita Degli Studi Di Roma, Wiley Online Library on [25/01/2023]. See the Terms and Conditions (https://onlinelibrary.wiley.com/terms-and-conditions) on Wiley Online Library for rules of use; OA articles are governed by the applicable Creative Commons License

16163028, 2022, 37, Downloaded from https://onlinelibrary.wiley.com/doi/10.1002/adfm.202201881 by Universita Degli Studi Di Roma, Wiley Online Library on [25/01/2023]. See the Terms and Conditions (https://onlinelibrary.wiley.com/terms-and-conditions) on Wiley Online Library for rules of use; OA articles are governed by the applicable Creative Commons License

(Figure S3, Supporting Information) for the target were observed with the lowest scaffold concentration (25×10^{-9} M). On the other hand, sensors fabricated using higher concentrations of DNA scaffold probe displayed lower signal gains and higher dissociation constants (K_D) against their target antibody (Figure S3, Supporting Information). The overall data therefore confirm that the signal-transduction mechanism of our sensor is based on a collisional mechanism.

2.3. Sensor Characterization

The specific architecture of the Y-shaped DNA scaffold receptor leads to a superior analytical performance compared to classical DNA scaffold sensors. To demonstrate this, we designed three new variants in order to induce a floppier structure with a higher conformational variability. The aim was to enhance the flexibility of the two recognition arms and affect the bivalent binding process with the target antibody (Figure 3A). To achieve these new variants, we kept the same sequences, and changed the single strand poly(T) core and location of the recognition elements. Specifically, the first variant, called the "modular variant", has four strands, where the recognition strand is substituted by two, non-connected "stem" portions (Figure 3A, red variant). This architecture allows for a higher degree of mobility of the two arms, which inevitably affects the conformational dynamics of the recognition elements. The second is the "modular internal variant", which is like the previous one, but with the recognition elements (digoxigenin) exposed in the inner part of the structure, thus in contact with each other (Figure 3A, blue variant).This architecture mimics the classic DNA-scaffold sensor where there is only a single recognition element for each probe (i.e., the two epitopes being so close to each other, only one paratope can bind) while keeping the Y-shaped structure, which facilitates the comparison with the native variant.[28] Finally, the third is the "control variant", which has the same structure as the original one, but without the digoxigenin molecules, and therefore, it is not able to bind the target (Figure 3A, black variant). Before testing our electrochemical sensors fabricated with the three different scaffold variants, their assembly was verified by PAGE (Figure 3B, lane 5,6, 7, and 8). This electrophoresis experiment showed four distinct bands with a similar mobility corresponding to each of the variants. This confirmed that all Y-shaped structures can be assembled with the same efficiency because they share the same sequences (Figure 2B). Finally, to demonstrate the different flexibility/stiffness of the variants, we performed a PAGE using a higher voltage (200 V) (Figure S4, Supporting Information). Under these conditions, the control and the native variant (Figure S4 (Supporting Information), lanes 1 and 4) displayed the same mobility, which was slightly lower than the modular variants (Figure S4 (Supporting Information), lanes 2, and 3). This could be due to the higher stiffness of the structures formed only by three strands with respect to the floppier and flexible modular variants formed by four strands.

After confirming the correct assembly of the Y-shaped DNA-scaffold receptors, we fabricated the electrochemical sensors and tested them by collecting their voltammetric signals with increasing concentrations of the anti-digoxigenin antibody target (Figure 3C,D). We found that the original and modular variants produce a Langmuir isotherm binding curve, and their signal can be related to the amount of target antibody present in solution (Figure 3A,C; red, green, and blue curves). The native variant produced the largest signal change (up to $-42.9 \pm 1.1\%$) and the highest affinity (K_D $2.2 \pm 0.3 \times 10^{-9}$ M; Figure 3C, green curve). On the other hand, the two modular variants produced a lower signal change (≈–25%) and showed lower affinities (K_Ds of $20.5 \pm 9.5 \times 10^{-9}$ M and $18.0 \pm 1.4 \times 10^{-9}$ M, for the modular variant and the modular internal variant, respectively) (Figure 3C, red and blue curves). We believe these data support our initial hypothesis and can be further explained considering two main factors. First, in the more constrained and stiffer native variant, the arms have a lower conformational variability (keeping the two epitopes always at a distance, which facilitates their recognition by the two paratopes), which helps the bivalent binding of the antibody (higher affinity). In the case of the modular variants, since the arms are free to move, they display a higher conformational dynamic that negatively affects the binding with the two paratopes. This could lead to an alternative binding process where two antibodies bind one single scaffold receptor (lower affinity). Second, because the modular variants share recognition arms with a higher flexibility, their high conformational dynamics increases the electron transfer between the methylene blue molecules and the electrode surface, leading to a higher background signal and lower signal gain. Finally, we tested the "control variant" which, as expected, did not produce any measurable electrochemical signal change for any of the concentrations of antibody used (up to 300×10^{-9} M; Figure 3C, black curve). The outcome of these experiments proved that the native variant is indeed the one that gives the best analytical performance.

The new Y-shaped DNA-based scaffold sensors are sensitive and selective. The anti-DIG antibody sensors respond sensitively to their target at low-nanomolar concentrations, displaying a useful dynamic range of 0.3 to 18×10^{-9} M (**Figure 4**A; green curve). The sensing platform also exhibits specificity, as it does not respond to non-targeted antibodies and proteins. To demonstrate this, we challenged it against anti-DNP antibodies and streptavidin (Figure 4A; red and blue curves). As expected, no measurable electrochemical signal was observed, not even in the presence of 300×10^{-9} M of anti-DNP antibodies and streptavidin. This indicates that the response obtained using anti-DIG antibodies is due to the specific recognition of the antigens. To further confirm the multivalent binding between the receptor and the target antibody, we used the anti-DIG Fab fragment as a target. We chose this antibody fragment because it displays a single paratope (i.e., does not exhibit any multivalent behavior) and lower molecular weight (≈50 kDa reducing the steric hindrance induced by the binding) than the IgGs (≈150 kDa).[59] As expected, the use of the anti-DIG Fab fragment produced a lower signal change ($-31.7 \pm 1.7\%$) and a lower affinity (K_D $4.8 \pm 1.9 \times 10^{-9}$ M) than those observed with the complete, bivalent antibody.

Our sensing platform is not only sensitive and specific, but also rapid, and enables the single-step detection of the target in untreated biological fluids. To characterize the sensor's equilibration time constant, we challenged our sensors using three different concentrations of anti-DIG antibodies: 1, 10, and

© 2022 The Authors. Advanced Functional Materials published by Wiley-VCH GmbH

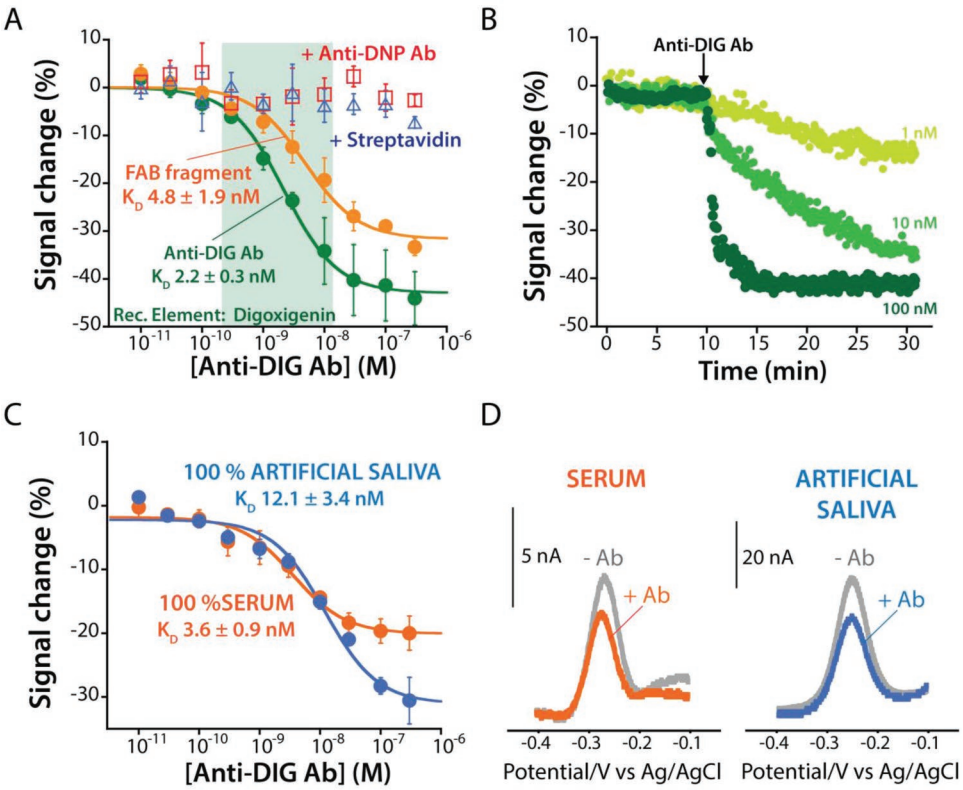

Figure 4. A) The sensor shows excellent sensitivity and specificity, as it is non-responsive to the presence of anti-DNP antibodies and streptavidin. At the same time, the sensor detects anti-DIG antibodies at low nanomolar concentrations (green curve). To test its performance against monovalent targets, we challenged the sensor against anti-DIG Fab, which produces a lower signal change and sensitivity than those achieved using the full anti-DIG IgG (orange curve). B) The sensor responds rapidly to the presence of anti-DIG antibodies. C) The sensor supports the single-step detection of the target working directly in undiluted matrices including artificial saliva (blue line) and serum (orange line), showing efficient nanomolar detection of the selected target antibody. The error bars reflect standard deviations derived using at least three independently fabricated sensors. D) Representative square wave voltammograms collected in the absence (gray) and in the presence of the antibody target (colored), for the different biological fluids (for the detection of 100×10^{-9} M anti-digoxigenin antibody in serum and artificial saliva).

100×10^{-9} M (Figure 4B). Fitting the binding kinetics to a single exponential decay, we estimated a time constant of 56.3 ± 1.7 s with 100×10^{-9} M antibody, 11.3 ± 0.4 min with 10×10^{-9} M, and 20.4 ± 3.3 min with 1×10^{-9} M: these values show that the response is sufficiently rapid to use the sensor at the point of care. We then characterized the sensor response in undiluted serum and artificial saliva (Figure 4C,D, blue curve) spiking increasing concentrations of anti-DIG antibodies from 10×10^{-12} M to 300×10^{-9} M. Even in the presence of these undiluted, complex biological matrices, the sensor promptly responded to the presence of the target in the nanomolar range. More specifically, using undiluted artificial saliva, we obtained a maximum signal change of –28.8 ± 1.9% and a K_D of 12.1 ± 3.4 × 10^{-9} M (Figure 4C,D, blue curve). When using undiluted serum, we obtained a maximum signal change of –18.3 ± 0.9% and a K_D of 3.6 ± 0.9 × 10^{-9} M (Figure 4C, orange curve).

To demonstrate the generalizability of our sensing platform, we fabricated sensors employing different recognition elements. Specifically, we replaced the DIG molecules at the ends of the recognition strand with two dinitrophenols (DNP) for the detection of the anti-DNP antibodies (**Figure 5**A–C). For this sensor, we observed a maximum signal change of –71.4 ± 2.1% and a K_D of 4.2 ± 0.5 × 10^{-9} M, thus showing a comparable performance to the previous system and to previous studies. [33,60] As expected, the native variant displays higher analytical performance than the modular variant (Figure S5, Supporting Information). As previously demonstrated (Figure 3), this is due to the shape of the target which is a bivalent immunoglobulin antibody. Again, the sensors are sufficiently specific to support clinically relevant measurements. They do not respond significantly when challenged with their protein interferants (Figure 5A) and they can work perfectly in undiluted biological fluids, such as serum and artificial saliva. Specifically, for the DNP system, in artificial saliva the sensor produced a maximum signal change of –42.5 ± 3.0% and a K_D of 6.7 ± 2.0 × 10^{-9} M; while in serum, it produced a maximum signal change of –28.2 ± 1.6% and a K_D of 3.0 ± 0.8 × 10^{-9} M (Figure 5B). As observed for the previous system, however, the gain under these circumstances was lower. We believe this is due to the presence of interferant proteins that can non-specifically adsorb on the surface,[29] thus affecting the collisional activity of the receptors, but not its recognition properties.

Last, we further demonstrated the programmability of the platform by expanding the set of biomolecular targets that can be detected with a single-step measurement. We thus selected the multivalent protein streptavidin as the target, and we

© 2022 The Authors. Advanced Functional Materials published by Wiley-VCH GmbH

16163028, 2022, 37, Downloaded from https://onlinelibrary.wiley.com/doi/10.1002/adfm.202201881 by Universita Degli Studi Di Roma, Wiley Online Library on [25/01/2023]. See the Terms and Conditions (https://onlinelibrary.wiley.com/terms-and-conditions) on Wiley Online Library for rules of use; OA articles are governed by the applicable Creative Commons License

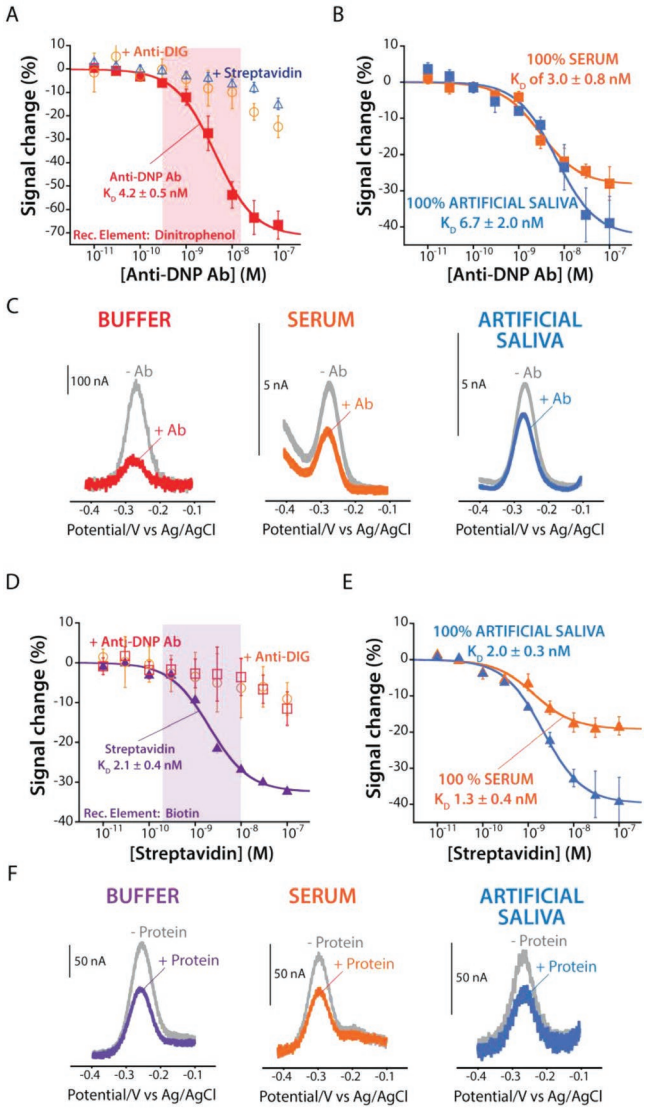

Figure 5. New targets can be detected by changing the recognition elements located in the arms of the scaffold receptor. A) We characterized the specificity of a Y-shaped DNA-scaffold sensor presenting two dinitrophenol (DNP) molecules as recognition elements. The results obtained confirmed the specific response only in the presence of the selected anti-DNP antibodies. B) The sensor responded promptly to the antibody target when challenged in undiluted serum (orange line) and artificial saliva (blue line). C) Representative square wave voltammograms collected in the absence (gray) and in the presence of the antibody target (colored), for the different matrices (for the detection of 100×10^{-9} M anti-digoxigenin antibody in buffer, serum and artificial saliva). D) Similarly, we fabricated a Y-shaped DNA-scaffold sensor presenting two biotin molecules to program its binding with the multivalent protein streptavidin. Again, the sensor only responded to the presence of the protein target. E) The platform enables the single-step detection of the selected target, and also worked in undiluted serum (orange line) and artificial saliva (blue line). Both sensors therefore respond to their specific target at low nanomolar concentrations with a high specificity and accuracy. The error bars reflect standard deviations derived using at least three independently fabricated sensors. F) Representative square wave voltammograms collected in the absence (gray) and in the presence of the proteiin target (colored), for the different matrices (for the detection of 100×10^{-9} M anti-digoxigenin antibody in buffer, serum and artificial saliva).

modified the recognition strand with two biotin molecules. As with the previous sensor, the resulting sensor is specific and selective and can detect the selected target at low nanomolar concentrations (Figure 5D,F, purple curve). The streptavidin sensor displays a signal gain of −32.5 ± 1.2% and a K_D of $2.1 \pm 0.4 \times 10^{-9}$ M. Conversely, for this protein target, the modular variant displays a higher signal gain and affinity than the native receptor (Figure S6, Supporting Information). This difference can be explained by considering the structure of the streptavidin where the two binding sites on the same face are ≈2.0 nm apart.[61,62] This distance is very small and only the flexibility of the modular variant can support a bivalent binding with the streptavidin. The sensor proved to be specific and to work perfectly with untreated biological fluids (Figure 5E,F). When it was challenged in artificial saliva, we observed a maximum signal change of −32.5 ± 1.2% and a K_D of $2.0 \pm 0.3 \times 10^{-9}$ M. On the other hand, in serum it produced a maximum signal change of −19.1 ± 1.3% and a K_D of $1.3 \pm 0.4 \times 10^{-9}$ M. These results confirm the ability of the platform to detect different molecular targets with the same efficiency and accuracy.

3. Conclusions

Exploiting the programmability of DNA as a nanomaterial and the multivalent binding properties of natural antibodies, we have developed a generalizable, programmable, and versatile electrochemical sensing platform for the single-step detection of biomolecular targets. We designed a Y-shaped DNA "scaffold" nanostructure that mimics the shape and the conformational variability of IgG bivalent antibodies. To adapt it to support electrochemical readouts and to detect the selected target, we modified the nanostructure with a thiol group and redox tag molecules, and two specific recognition elements that can be changed in relation to the selected target. The binding of the target antibody or protein with the recognition molecules leads to the formation of a bulky target-receptor complex that reduces the collisional dynamics of the Y-shaped DNA nanostructure, producing a decrease in the faradic current that is related to the concentration of the target. This novel DNA scaffold sensor enables, in principle, the detection of any biomolecular target for which two recognition molecules can be incorporated into the sequence of the anchoring strand. To prove this, we used our sensing platform to quantitively detect two bivalent antibody targets and one multivalent protein target. The sensor can rapidly (in <15 min) detect such targets at low nanomolar concentrations with a high specificity. Lastly, we demonstrated the robustness of our Y-shaped scaffold sensor by detecting selected biomolecular targets in complex biological fluids, such as serum and artificial saliva. Despite the sensor can detect the targets in a single step in these biological fluids, artificial saliva does not have the same complexity as a pooled human saliva sample. This represents a limitation of this study; therefore, further tests need to be performed to characterize and optimize the sensor in real saliva.

The development of the electrochemical Y-shaped scaffold sensor offers a new analytical tool compared to the existing methods for detecting biomolecules. For example, the lack of an enzymatic amplification step makes our platform less sensitive than ELISA[8] or other sensing approaches based on the

© 2022 The Authors. Advanced Functional Materials published by Wiley-VCH GmbH

16163028, 2022, 37, Downloaded from https://onlinelibrary.wiley.com/doi/10.1002/adfm.202201881 by Universita Degli Studi Di Roma, Wiley Online Library on [25/01/2023]. See the Terms and Conditions (https://onlinelibrary.wiley.com/terms-and-conditions) on Wiley Online Library for rules of use; OA articles are governed by the applicable Creative Commons License

co-localization or binding-induced conformational changes that can trigger and modulate enzymatic activity.[54,63,64] Despite this, the signal transduction mechanism of our sensor makes the detection of the target reagentless, rapid, and single-step that is crucial for high-frequency testing. In fact, to perform the measurement, there is no need for washing or incubation, or the addition of reagents, and there is no risk of environmental factors affecting the enzymatic catalysis. The analytical performance of our platform compares well with previously engineered DNA-based electrochemical sensors[24,27,33,54] and more recently developed optical homogeneous assays.[55,63,65–68] Our electrochemical Y-shaped scaffold sensor could be further improved to support mass testing, for example, using calibration-free and dual reporter approaches (i.e., allowing the direct quantification of the target).[69–72] It could also be easily integrated with mobile phones or portable electrochemical setups, thus, offering a more efficient tool for real-time epidemiology.[69]

4. Experimental Section

Chemical Reagents and Materials: Reagent-grade chemicals, including phosphate buffered saline tablets (PBS), sodium hydroxide (NaOH), hydrochloric acid (HCl), 6-mercapto-1-hexanol, sodium chloride (NaCl), ethanol (CH_3CH_2OH), magnesium chloride ($MgCl_2$), tris(2-carboxyethyl)-phosphine hydrochloride (TCEP), tris[hydroxymethyl]-aminomethane hydrochloride (Trizma), ethylenediaminetetraacetic acid (EDTA), and 100% Human Serum (H4522-100ML) were obtained from Sigma-Aldrich (St. Louis, MO, USA), and were used as received. Sulfuric acid 96% (H_2SO_4) was obtained from Panreac Química S.L.U. (Barcelona, Spain). Antibody targets such as digoxigenin (DIG) sheep polyclonal antibody (500 µL of 5 mg mL^{-1} solution; ab64509) were purchased from Abcam (Germany), while 2,4-dinitrophenol (DNP) goat polyclonal antibody (1 mL of 1 mg mL^{-1} solution; 17 160 209) was purchased by Fischer Scientific (Madrid, Spain). The antibodies were stored at −20 and 4 °C respectively and diluted in PBS (NaCl 137×10^{-3} M, KCl 2.7×10^{-3} M, Na_2HPO_4 10×10^{-3} M, KH_2PO_4 1.8×10^{-3} M at pH 7.4) before their use. The anti-DIG antibody Fab fragment (1 mg) was obtained from Sigma-Aldrich (St. Louis, MO, USA) in lyophilized form. It was dissolved in PBS to reach a concentration of 1 mg mL^{-1} and stored at 4 °C. The Streptavidin (10 mg, 13.3 kDa for each subunit) protein target was purchased from Sigma-Aldrich (St. Louis, MO, USA) and was diluted in milliQ water to reach the final concentration of 145×10^{-6} M and stored at −20 °C. Artificial Saliva for Medical and Dental Research (Part number 1700-0305) was purchased from LCTech GmbH (Obertaufkirchen, Germany) and was used as received. The Ag|AgCl reference electrodes (CHI111/112 reference electrode) and platinum wire (CHI115 counter electrode) were purchased from CH Instruments (Austin, TX, USA).

Oligonucleotides: High-performance liquid chromatography purified oligonucleotides were purchased from Biomers GmbH (Ulm, Germany) and IBA Lifesciences (Göttingen, Germany) and were received in lyophilized form. The oligonucleotides were dissolved in TE buffer (10×10^{-3} M Tris buffer, 1×10^{-3} M EDTA, pH 7.8) at a concentration of 100×10^{-6} M and then aliquoted and stored at −20 °C. The final concentration of the oligonucleotides was verified using a Shimadzu mod. UV-1900 Spectrophotometer (Duisburg, Germany) and a TrayCell (optical path 0.02 cm) measuring the relative absorbance at 260 nm. All variants of the Y-shape DNA scaffold share the same sequences and were composed of the same Anchoring strand 1, Anchoring strand 2, while the recognition strand was the programmable part (Figure S1A, Supporting Information). Specifically, Anchoring strand 1 was modified with a thiol-C6-SS group at its 5′ end, and a methylene blue molecule at 3′ end, while Anchoring strand 2 was modified at 3′ end with a methylene blue molecule. The control and native variants (Figure 3A) had the same recognition strand sequence, which was not modified or modified with two molecular receptors (whether Epitope of Digoxigenin, Dinitrophenol or Biotin) at both 5′ and 3′ end. Modular and modular internal variants had the same two recognition strand sequences (recognition strand left and recognition strand right, which were modified with epitopes or biotin in 3′ or 5′ end, respectively).

The sequences and modification schemes are as follows:

Anchoring strand 1
5′-(OH-C6-SS)-GTCAACCTATCGTACTTGCG**TTTTT**GCTATGTCAACTGCG TCTAC-(Atto-MB2)-3′

Anchoring strand 2
5′-GCACTCTGATATGACAGACG**TTTTT**CGCAAGTACGATAGGT TGAC-(Atto-MB2)-3′

Recognition strand (DIG)
5′-(DIG)-GTAGACGCAGTTGACATAGC**TTTTT**CGTCTGTCATATCAGA GTGC-(DIG)-3′

Recognition strand (DNP)
5′-(DNP)-GTAGACGCAGTTGACATAGC**TTTTT**CGTCTGTCATATCAGA GTGC-(DNP)-3′

Recognition strand (Biotin)
5′-(Biotin)-GTAGACGCAGTTGACATAGC**TTTTT**CGTCTGTCATATCAGA GTGC-(Biotin)-3′

Recognition strand (control)
5′-GTAGACGCAGTTGACATAGC**TTTTT**CGTCTGTCATATCAGAGTGC-3′

Recognition strand Left (DIG), Modular variant.
5′-GTAGACGCAGTTGACATAGC-(DIG)-3′

Recognition strand Right (DIG), Modular variant.
5′-CGTCTGTCATATCAGAGTGC-(DIG)-3′

Recognition strand Left (DNP), Modular variant.
5′-GTAGACGCAGTTGACATAGC-(DNP)-3′

Recognition strand Right (DNP), Modular variant.
5′-CGTCTGTCATATCAGAGTGC-(DNP)-3′

Recognition strand Left (Biotin), Modular variant.

5′-GTAGACGCAGTTGACATAGC-(Biotin)-3′
Recognition strand Right (DNP), Modular variant.

5′-CGTCTGTCATATCAGAGTGC-(Biotin)-3′

Recognition strand Left (DIG), Modular internal variant.

5′-(DIG)-GTAGACGCAGTTGACATAGC-3′

Recognition strand Right (DIG), Modular internal variant.
5′-(DIG)-CGTCTGTCATATCAGAGTGC-3′

The sequences in bold represent the poly(T) portion.

NUPACK Simulations: NUPACK was used (http://www.nupack.org/) to predict the folding of the DNA single strands Anchoring strand 1, Anchoring strand 2, and the recognition strand (Figure S1, Supporting Information).[47] First, the oligo sequences were analyzed using the NUPACK to predict their native folding and the absence of stable secondary structure. Then the sequences to confirm the correct assembly of the double stranded "stem" portions and the Y-shaped nanostructure were progressively combined. To perform the analysis following parameters were used: a) temperature: 25 °C; b) number of strand species: 1, 2, and 3; c) maximum complex size: 4; d) oligo concentration = 500×10^{-9} M; in advanced options; e) [Na+] = 0.15 M, [Mg++] = 0 M; f) dangle treatment: some.

Gold Wire Electrode Fabrication and Electrochemical Cleaning: To perform the in-vitro characterization of our Y-shaped scaffold sensors (Figures 3, 4, and 5; Figures S2, S3, S5, and S6, Supporting Information), these were fabricated following an established approach.[19,73] Briefly, segments of bare gold wire with a diameter of 200 µm (99.9% Metals

© 2022 The Authors. Advanced Functional Materials published by Wiley-VCH GmbH

16163028, 2022, 37, Downloaded from https://onlinelibrary.wiley.com/doi/10.1002/adfm.202201881 by Universita Degli Studi Di Roma, Wiley Online Library on [25/01/2023]. See the Terms and Conditions (https://onlinelibrary.wiley.com/terms-and-conditions) on Wiley Online Library for rules of use; OA articles are governed by the applicable Creative Commons License

basis – Alfa Aesar, Ward Hill, MA, U.S.A.) were cut (5.5 cm in length), and the insulated body of the wires was coated using at least two layers of heat-shrink polytetrafluoroethylene insulation tubing (PTFE, HS Sub-Lite-Wall, 0.02 ± 0.001 in, black opaque). To connect with the potentiostat, a gold pin (item CHI_PIN; CH Instruments, Austin, TX, USA) was soldered to one end of the electrode, and this contact was further coated with insulating connector paint (MG Chemicals, Burlington, ON, Canada). To perform the functionalization of the electrode, the uninsulated end of the gold wire to a final length of 3.5 mm was cut.Then, An electrochemical cleaning of this uninsulated portion using the following two-step protocol was performed: 1) 1000–1500 cycles between –1 and –1.6 V in a solution of 0.5 M NaOH at 1 V s^{-1} to remove any residual thiol/organic contaminants on the electrode surface and 2) pulsed between 0 and 2 V for at least 16 000 cycles with a pulse length of 20 ms (no waiting between pulses) in 0.5 M H_2SO_4 to increase the electrode roughness, as previously reported.[19,73]

Electrode Functionalization: The cleaned gold wire electrodes were functionalized with the assembled DNA scaffold nanostructure. Specifically, for the Native variant (Figures 2, 3, 4, and 5; Figures S2, S3, S5, and S6, Supporting Information) and Control Variant (Figure 3C), the following protocol were used: 1) The recognition strand and Anchoring strand 2 were diluted separately with the assembling buffer (10×10^{-3} M sodium phosphate, 1 M NaCl, 1×10^{-3} M $MgCl_2$, pH 7.3) to reach a concentration of 3×10^{-6} M. For their assembly, these were mixed using the same volume to obtain a final concentration of 1.5×10^{-6} M. This solution was heated to 90 °C for 5 min and then cooled to room temperature for 1 h. 2) At the same time, the Anchoring strand 1 (100×10^{-6} M) was treated with 10×10^{-3} M tris(2-carboxyethyl)-phosphine hydrochloride (TCEP; dissolved in milliQ water) for 1 h at room temperature in the dark. 3) After this incubation step, the Anchoring strand 1 was diluted with the assembling buffer to reach a final concentration of 3×10^{-6} M. Next, an aliquot of this solution was added to the previous solution containing the Recognition strand and Anchoring strand 2, to obtain a solution with the three modified oligos at a 1:1:1 molar ratio and a concentration of 1×10^{-6} M. Finally, the authors waited 20 min for them to assemble.

For the Modular (Figure 3; Figures S5 and S6, Supporting Information) and Modular internal variant (Figure 3C) the following protocol were used: 1) the Anchoring strand 2 and Recognition strand right were diluted separately with assembling buffer to reach a concentration of 4×10^{-6} M. Next, they were mixed to obtain a final concentration of 2×10^{-6} M. This solution was heated to 90 °C for 5 min and then allowed to cool to room temperature for 1 h. 2) At the same time, the Anchoring strand 1 (2 µL) oligonucleotide was treated with 4 µL of 10×10^{-3} M TCEP in Tris solution for 1 h at room temperature and in the dark. 3) After this incubation step, the Anchoring strand 1 was diluted with assembling buffer until it reached a concentration of 4×10^{-6} M, and the Recognition strand left solution (4×10^{-6} M) was added to obtain a final solution (Anchoring strand 1 + Recognition strand left) with a concertation of 2×10^{-6} M. The authors waited 5 min to let them assemble. 4) Finally, the two solutions were mixed to achieve a final solution containing the four modified oligos at a 1:1:1:1 molar ratio and a concentration of 1×10^{-6} M. Finally, the authors waited 20 min for them to assemble. The electrochemically cleaned gold wire electrodes were then immersed in 200 µL of these solutions (containing the assembled Y-shaped receptor) for 1 h in the dark. The electrode surface was then rinsed with distilled water and incubated overnight at 4 °C in assembling buffer containing 5×10^{-3} M 6-mercaptohexanol, followed by a further rinse with distilled water before use.

Electrochemical Experiments: Electrochemical measurements were performed in a standard three-electrode cell setup containing an Ag/AgCl (3 M KCl) reference electrode and platinum counter electrode, using a CHI1030C Multiplexer (CH Instruments, Austin, TX, USA) at room temperature. Square Wave Voltammetry (SWV) was performed using a potential window of –0.10 to –0.42 V, a potential step of 0.001 V and 0.025 V amplitude.

Frequency Map: To characterize the sensing mechanism of our electrochemical platform, the SWV frequency dependence of the scaffold sensors' signal gain (relative signal change when challenged with the saturating target; Figure S2, Supporting Information) was determined. For this, at least three sensors in the absence and presence of a saturating concentration of the anti-DIG antibody (100×10^{-9} M) were interrogated. The peak currents estimated in the absence of the target correspond to $I^{\circ}_{cVariant}$ values, while the peak currents estimated in the presence of the target correspond to $I^{[Target]}_{cVariant}$. These raw current values have been converted to relative signal change $I^{\%signal}_{cVariant}$ using the approach described below andin Equation 2, and it had been performed for each SWV frequency tested.[57,74,75] In addition, to understand the effect of the density of the DNA scaffold receptor on the signal gain and the sensitivity of the sensors, their electrode surface was functionalized with different concentrations of the native variant receptor (25, 75, 150, and 300×10^{-9} M).

Binding Curve: Experimental binding curves were performed in 9 mL of working buffer (537×10^{-3} M NaCl, 2.7×10^{-3} M KCl, 10×10^{-3} M Na_2HPO_4, 1.8×10^{-3} M KH_2PO_4, at pH 7.4) (Figures 3C, 4A, and 5A,C; Figures S3, S5, and S6, Supporting Information) or in 9 mL artificial saliva (Figures 4C and 5B,D), or in 9 mL of human serum (Figures 4C and 5B,D). For each titration test, at least three gold wire electrodes modified with the native variant (Figures 3C, 4, and 5; Figures S3, S5, and S6, Supporting Information) or control variant (Figure 3C), or with the modular variant (Figures 3C; Figures S5 and S6, Supporting Information) or internal modular variant (Figure 3C) were used. More specifically, in the absence of the protein target or interferents, a preliminary treatment was performed in the working buffer (or in the selected biological fluids) by interrogating the sensors with 30–60 scans until stable peak currents were obtained. Once the scaffold sensor's signal was stable, increasing concentrations of the selected antibody or protein were added to the working solution at 20 min intervals and the sensors were interrogated. The SWV signals were collected using a frequency of 90 Hz except for the binding curves obtained in serum and artificial saliva (Figure 4C,D) where a frequency of 5 Hz and 30 Hz, respectively was used. The peak current of the scaffold sensor at each concentration of target was extracted using a recently published script written in Python that analyzes the voltametric data by subtracting the baseline current from the peak maxima ($I^{[Target]-MAx}_{cVariant}$).[74] The resulting data were fitted using a Langmuir equation (single-site binding)[76] in Kaleidagraph (Synergy Software).

$$I^{[Target]}_{cVariant} = I^{\circ}_{cVariant} + \left(\frac{[target]\left(I^{[Target]-MAx}_{cVariant} - I^{\circ}_{cVariant}\right)}{[target] + K_D} \right) \quad (1)$$

where [target] is the concentration of the antibody or protein target, $I^{[Target]}_{cVariant}$ is the raw signal current in the presence of protein target, $I^{\circ}_{cVariant}$ is the background raw current seen in the absence of the target, $I^{[Target]-MAx}_{cVariant}$ is the raw current signal change seen at saturating target concentrations, and $K_D$is the dissociation constant of the surface-bound DNA scaffold receptor.

Using the $I^{\circ}_{cVariant}$ values estimated from the fit, the raw signalling current of each sensor into the relative signal change $I^{\%signal}_{cVariant}$ using the following equation was converted:

$$I^{\%signal}_{cVariant} = \left(\frac{I^{[Target]}_{cVariant} - I^{\circ}_{cVariant}}{I^{\circ}_{cVariant}} \right) \times 100 \quad (2)$$

Sensor Equilibration Time: The scaffold sensor's equilibration time was determined (Figure 4B) using the above experimental approach and interrogating the sensor every 5 s at 90 Hz in a working buffer (537×10^{-3} M NaCl, 2.7×10^{-3} M KCl, 10×10^{-3} M Na_2HPO_4, 1.8×10^{-3} M KH_2PO_4, at pH 7.4). More specifically, after obtaining a stable current baseline (10 min), three different concentrations of anti-DIG antibody to the solution (1, 10, and 100×10^{-9} M) were added, and then the voltammetric signal was monitored for over 20 min. Using the previously cited Python script,[74] the data were analyzed using Equation 2 and converted the raw current into the relative % signal change. The observed signal change was then fitted to a single exponential decay

© 2022 The Authors. Advanced Functional Materials published by Wiley-VCH GmbH

16163028, 2022, 37, Downloaded from https://onlinelibrary.wiley.com/doi/10.1002/adfm.202201881 by Universita Degli Studi Di Roma, Wiley Online Library on [25/01/2023]. See the Terms and Conditions (https://onlinelibrary.wiley.com/terms-and-conditions) on Wiley Online Library for rules of use; OA articles are governed by the applicable Creative Commons License

in KaleidaGraph (Synergy Software) to obtain the equilibration time constant of the sensor.

Native PAGE Experiments: The correct DNA strand assembly was evaluated by gel native PAGE electrophoresis (Figures 2B and 3B; Figures S4, Supporting Information) using 20% TBE polyacrylamide gels (Invitrogen, ThermoFisher Scientific, Carlsbad, California, USA). Electrophoresis was performed in 1X TBE buffer at 150 V (Figures 2B and 3B) (or 200 V; Figure S4, Supporting Information) for 120 min in a Cell SureLock Mini-cell chamber (ThermoFisher Scientific, Waltham, Massachusetts, USA). GeneRuler Ultra Low Range was used as the molecular weight marker (ThermoScientific, Waltham, Massachusetts, USA). The gel was stained with SYBR Gold (dissolved in 1X TBE buffer) for 20 min (Thermo Fisher Scientific, Waltham, Massachusetts, USA), then scanned using a Biodoc-H Imaging System transilluminator (Somatco, Riyadh, Saudi Arabia) in combination with TS Software.

Supporting Information

Supporting Information is available from the Wiley Online Library or from the author.

Acknowledgements

A..I. and A..B. contributed equally to this work. ICN2 was funded by the CERCA programme, Generalitat de Catalunya. ICN2 was supported by the Severo Ochoa Centres of Excellence programme and funded by the Spanish Research Agency (AEI, grant no. SEV-2017-0706). The authors acknowledge Consejo Superior de Investigaciones Científicas (CSIC) for the project "COVID19-122" granted in the call "Nuevas ayudas extraordinarias a proyectos de investigación en el marco de las medidas urgentes extraordinarias para hacer frente al impacto económico y social del COVID-19 (Ayudas CSIC-COVID-19)". A.I. was supported by PROBIST postdoctoral fellowship funded by the European Research Council (Marie Skłodowska-Curie grant agreement no. 754510). C.P. acknowledges the Marie Skłodowska-Curie Actions Individual Fellowship; this project received funding from the European Union's Horizon 2020 research and innovation programme under the Marie Skłodowska-Curie grant agreement No. 795635. C.P. (ISGlobal) also acknowledges support from the Spanish Ministry of Science and Innovation** and State Research Agency through the "Centro de Excelencia Severo Ochoa 2019–2023" Program (CEX2018-000806-S), and support from the Generalitat de Catalunya through the CERCA Program. R.A.D. received financial support from the EU Graphene Flagship Core 3 Project (No. 881603).

Conflict of Interest

The authors declare no conflict of interest.

Data Availability Statement

The data that support the findings of this study are available from the corresponding author upon reasonable request.

Keywords

antibody detection, DNA-scaffolds, nature-inspired biosensors, protein detection, serology, square wave voltammetry

Received: February 16, 2022
Revised: May 31, 2022
Published online: June 22, 2022

[1] J. T. Ladner, N. D. Grubaugh, O. G. Pybus, K. G. Andersen, *Nat. Med.* **2019**, *25*, 206.
[2] Z. Meng, S. Guo, Y. Zhou, M. Li, M. Wang, B. Ying, *Signal Transduct. Target. Ther.* **2021**, *6*, 1.
[3] A. Poschenrieder, M. Thaler, R. Junker, P. B. Luppa, *Anal. Bioanal. Chem.* **2019**, *411*, 7607.
[4] C. S. Wood, M. R. Thomas, J. Budd, T. P. Mashamba-Thompson, K. Herbst, D. Pillay, R. W. Peeling, A. M. Johnson, R. A. McKendry, M. M. Stevens, *Nat. 2019 5667745* **2019**, *566*, 467.
[5] A. N. M. Kraay, K. N. Nelson, C. Y. Zhao, D. Demory, J. S. Weitz, B. A. Lopman, *Nat. Commun.* **2021**, *12*, 7063.
[6] C. Royo-Cebrecos, D. Vilanova, J. López, V. Arroyo, M. Pons, G. Francisco, M. G. Carrasco, J. M. Piqué, S. Sanz, C. Dobaño, A. L. García-Basteiro, *Lancet Reg. Heal. – Eur.* **2021**, *5*, 100119.
[7] G. Rosati, A. Idili, C. Parolo, C. Fuentes-Chust, E. Calucho, L. Hu, C. D. C. Castro E Silva, L. Rivas, E. P. Nguyen, J. F. Bergua, R. Alvárez-Diduk, J. Muñoz, C. Junot, O. Penon, D. Monferrer, E. Delamarche, A. Merkoçi, *ACS Nano* **2021**, *15*, 17137.
[8] C. Parolo, A. S. Greenwood, N. E. Ogden, D. Kang, C. Hawes, G. Ortega, N. Arroyo-Currás, K. W. Plaxco, *Microsystems Nanoeng.* **2020**, *6*, 13.
[9] R. M. Lequin, *Clin. Chem.* **2005**, *51*, 2415.
[10] E. Engvall, *Clin. Chem.* **2010**, *56*, 319.
[11] K. J. Land, D. I. Boeras, X. S. Chen, A. R. Ramsay, R. W. Peeling, *Nat. Microbiol.* **2019**, *4*, 46.
[12] C. Parolo, A. Sena-Torralba, J. F. Bergua, E. Calucho, C. Fuentes-Chust, L. Hu, L. Rivas, R. Álvarez-Diduk, E. P. Nguyen, S. Cinti, D. Quesada-González, A. Merkoçi, *Nat. Protoc.* **2020**, *15*, 3788.
[13] A. Clifford, J. Das, H. Yousefi, A. Mahmud, J. B. Chen, S. O. Kelley, *J. Am. Chem. Soc.* **2021**, *143*, 5281.
[14] S. Ranallo, A. Porchetta, F. Ricci, *Anal. Chem.* **2019**, *91*, 44.
[15] A. B. Bezerra, A. S. N. Kurian, C. J. Easley, *Anal. Chem.* **2021**, *93*, 198.
[16] Y. Xiao, A. A. Lubin, A. J. Heeger, K. W. Plaxco, *Angew. Chemie – Int. Ed.* **2005**, *44*, 5456.
[17] R. Y. Lai, K. W. Plaxco, A. J. Heeger, *Anal. Chem.* **2007**, *79*, 229.
[18] C. Parolo, A. Idili, G. Ortega, A. Csordas, A. Hsu, Q. Yang, B. S. Ferguson, J. Wang, K. W. Plaxco, N. N. Arroyo-Currás, Q. Yang, B. S. Ferguson, J. Wang, K. W. Plaxco, *ACS Sens.* **2020**, *5*, 1877.
[19] A. Idili, C. Parolo, R. Alvarez-Diduk, A. Merkoçi, *ACS Sens.* **2021**, *6*, 3093.
[20] A. Idili, J. Gerson, T. Kippin, K. W. Plaxco, *Anal. Chem.* **2021**, *93*, 4023.
[21] A. Idili, J. Gerson, C. Parolo, T. Kippin, K. W. K. W. Plaxco, *Anal. Bioanal. Chem.* **2019**, *411*, 4629.
[22] A. Vallée-Bélisle, K. W. Plaxco, *Curr. Opin. Struct. Biol.* **2010**, *20*, 518.
[23] N. Arroyo-Currás, P. Dauphin-Ducharme, K. Scida, J. L. Chávez, *Anal. Methods* **2020**, *12*, 1288.
[24] A. Vallée-Bélisle, F. Ricci, T. Uzawa, F. Xia, K. W. Plaxco, A. Valle, *J. Am. Chem. Soc.* **2012**, *134*, 15197.
[25] A. Idili, F. Ricci, A. Vallée-Bélisle, *Nucleic Acids Res.* **2017**, *45*, 7571.
[26] M. Rossetti, S. Ranallo, A. Idili, G. Palleschi, A. Porchetta, F. Ricci, *Chem. Sci.* **2017**, *8*, 914.
[27] K. J. Cash, F. Ricci, K. W. Plaxco, *J. Am. Chem. Soc.* **2009**, *131*, 6955.
[28] R. J. White, H. M. Kallewaard, W. Hsieh, A. S. Patterson, J. B. Kasehagen, K. J. Cash, T. Uzawa, H. T. Soh, K. W. Plaxco, *Anal. Chem.* **2012**, *84*, 1098.
[29] N. E. Ogden, M. Kurnik, C. Parolo, K. W. Plaxco, *Analyst* **2019**, *144*, 5277.
[30] J. Das, S. Gomis, J. B. Chen, H. Yousefi, S. Ahmed, A. Mahmud, W. Zhou, E. H. Sargent, S. O. Kelley, *Nat. Chem.* **2021**, *13*, 428.
[31] H. Yousefi, A. Mahmud, D. Chang, J. Das, S. Gomis, J. B. Chen, H. Wang, T. Been, L. Yip, E. Coomes, Z. Li, S. Mubareka, A. Mcgeer, N. Christie, S. Gray-Owen, A. Cochrane, J. M. Rini, E. H. Sargent, S. O. Kelley, *J. Am. Chem. Soc.* **2021**, *134*, 1722.

© 2022 The Authors. Advanced Functional Materials published by Wiley-VCH GmbH

16163028, 2022, 37, Downloaded from https://onlinelibrary.wiley.com/doi/10.1002/adfm.202201881 by Universita Degli Studi Di Roma, Wiley Online Library on [25/01/2023]. See the Terms and Conditions (https://onlinelibrary.wiley.com/terms-and-conditions) on Wiley Online Library for rules of use; OA articles are governed by the applicable Creative Commons License

[32] D. Kang, C. Parolo, S. Sun, N. E. Ogden, F. W. Dahlquist, K. W. Plaxco, *ACS Sens.* **2018**, *3*, 1271.
[33] S. S. Mahshid, S. Camiré, F. Ricci, A. Vallée-Bélisle, *J. Am. Chem. Soc.* **2015**, *137*, 15596.
[34] G. Vidarsson, G. Dekkers, T. Rispens, *Front. Immunol.* **2014**, *5*, 520.
[35] H. Ma, R. O'Kennedy, *Methods Mol. Biol.* **2015**, *1348*, 7.
[36] N. C. Seeman, H. F. Sleiman, *Nat. Rev. Mater.* **2018**, *3*, 17068.
[37] N. C. Seeman, *Annu. Rev. Biochem.* **2010**, *79*, 65.
[38] D. Scalise, R. Schulman, *Annu. Rev. Biomed. Eng.* **2019**, *21*, 469.
[39] N. L. Goddard, G. Bonnet, O. Krichevsky, A. Libchaber, *Phys. Rev. Lett.* **2000**, *85*, 2400.
[40] D. Mariottini, A. Idili, M. A. D. Nijenhuis, T. F. A. De Greef, F. Ricci, *J. Am. Chem. Soc.* **2018**, *140*, 14725.
[41] F. Iacovelli, C. Alves, M. Falconi, F. Oteri, C. L. P. De Oliveira, A. Desideri, *Biopolymers* **2014**, *101*, 992.
[42] F. Iacovelli, M. Falconi, B. R. Knudsen, A. Desideri, *RSC Adv.* **2016**, *6*, 35160.
[43] P. Zhang, X. Liu, P. Liu, F. Wang, H. Ariyama, T. Ando, J. Lin, L. Wang, J. Hu, B. Li, C. Fan, *Nat. Commun.* **2020**, *E11*.
[44] S. Sandin, L. G. Öfverstedt, A. C. Wikström, Ö. Wrange, U. Skoglund, *Structure* **2004**, *12*, 409.
[45] J. Jay, B. Bray, Y. Qi, E. Igbinigie, H. Wu, J. Li, G. Ren, *Antibodies* **2018**, *7*, 18.
[46] X. Zhang, L. Zhang, H. Tong, B. Peng, M. J. Rames, S. Zhang, G. Ren, *Sci. Rep.* **2015**, *5*, 9803.
[47] J. N. Zadeh, C. D. Steenberg, J. S. Bois, B. R. Wolfe, M. B. Pierce, A. R. Khan, R. M. Dirks, N. A. Pierce, *J. Comput. Chem.* **2011**, *32*, 170.
[48] P. S. Kwon, S. Ren, S. J. Kwon, M. E. Kizer, L. Kuo, M. Xie, D. Zhu, F. Zhou, F. Zhang, D. Kim, K. Fraser, L. D. Kramer, N. C. Seeman, J. S. Dordick, R. J. Linhardt, J. Chao, X. Wang, *Nat. Chem.* **2020**, *12*, 26.
[49] C. Tian, C. Zhang, *Methods Mol. Biol.* **2017**, *1500*, 11.
[50] A. R. Chandrasekaran, *Nat. Rev. Chem.* **2021**, *5*, 225.
[51] D. Shu, Y. Shu, F. Haque, S. Abdelmawla, P. Guo, *Nat. Nanotechnol.* **2011**, *6*, 658.
[52] Y. Takezawa, S. Yoneda, J. L. H. A. Duprey, T. Nakama, M. Shionoya, *Chem. Sci.* **2016**, *7*, 3006.
[53] M. Galanti, D. Fanelli, F. Piazza, *Sci. Rep.* **2016**, *6*, 18976.
[54] M. Rossetti, S. Brannetti, M. Mocenigo, B. Marini, R. Ippodrino, A. Porchetta, *Angew. Chemie – Int. Ed.* **2020**, *59*, 14973.
[55] S. Ranallo, M. Rossetti, K. W. Plaxco, A. Vallée-Bélisle, F. Ricci, *Angew. Chemie – Int. Ed.* **2015**, *54*, 13214.
[56] P. Dauphin-Ducharme, K. W. Plaxco, *Anal. Chem.* **2016**, *88*, 11654.
[57] R. J. White, K. W. Plaxco, *Anal. Chem.* **2010**, *82*, 73.
[58] F. Ricci, R. Y. Lai, A. J. Heeger, K. W. Plaxco, J. J. Sumner, *Langmuir* **2007**, *23*, 6827.
[59] A. De La Escosura-Muñiz, C. Parolo, A. Merkoi, *Mater. Today* **2010**, *13*, 24.
[60] K. J. Cash, F. Ricci, K. W. Plaxco, *Chem. Commun. (Camb).* **2009**, *41*, 6222.
[61] W. A. Hendrickson, A. Pähler, J. L. Smith, Y. Satow, E. A. Merritt, R. P. Phizackerley, *Proc. Natl. Acad. Sci. USA* **1989**, *86*, 2190.
[62] C. L. Ren, D. Carvajal, K. R. Shull, I. Szleifer, *Langmuir* **2009**, *25*, 12283.
[63] A. Porchetta, R. Ippodrino, B. Marini, A. Caruso, F. Caccuri, F. Ricci, *J. Am. Chem. Soc.* **2018**, *140*, 947.
[64] R. Arts, I. Den Hartog, S. E. Zijlema, V. Thijssen, S. H. E. Van Der Beelen, M. Merkx, *Anal. Chem.* **2016**, *88*, 4525.
[65] D. Legendre, P. Soumillion, J. Fastrez, *Nat. Biotechnol.* **1999**, *17*, 67.
[66] L. Tian, T. Heyduk, *Anal. Chem.* **2009**, *81*, 5218.
[67] K. Tenda, B. van Gerven, R. Arts, Y. Hiruta, M. Merkx, D. Citterio, *Angew. Chemie – Int. Ed.* **2018**, *57*, 15369.
[68] K. J. Oh, K. J. Cash, A. A. Lubin, K. W. Plaxco, *Chem. Commun.* **2007**, *46*, 4869.
[69] G. Rosati, M. Urban, L. Zhao, Q. Yang, C. de Carvalho Castro e Silva, S. Bonaldo, C. Parolo, E. P. Nguyen, G. Ortega, P. Fornasiero, A. Paccagnella, A. Merkoçi, *Biosens. Bioelectron.* **2022**, *196*, 113737.
[70] A. Idili, C. Parolo, G. Ortega, K. W. Plaxco, *ACS Sens.* **2019**, *4*, 3227.
[71] H. Li, P. Dauphin-Ducharme, G. Ortega, K. W. Plaxco, *J. Am. Chem. Soc.* **2017**, *139*, 11207.
[72] Y. Du, B. J. Lim, B. Li, Y. S. Jiang, J. L. Sessler, A. D. Ellington, *Anal. Chem.* **2014**, *86*, 8010.
[73] N. Arroyo-Currás, K. Scida, K. L. Ploense, T. E. Kippin, K. W. Plaxco, *Anal. Chem.* **2017**, *89*, 12185.
[74] S. D. Curtis, K. L. Ploense, M. Kurnik, G. Ortega, C. Parolo, T. E. Kippin, K. W. Plaxco, N. Arroyo-Currás, *Anal. Chem.* **2019**, *91*, 12321.
[75] A. Idili, A. Amodio, M. Vidonis, J. Feinberg-Somerson, M. Castronovo, F. Ricci, *Anal. Chem.* **2014**, *86*, 9013.
[76] B. E. Fernández de Ávila, H. M. Watkins, J. M. Pingarrón, K. W. Plaxco, G. Palleschi, F. Ricci, *Anal. Chem.* **2013**, *85*, 6593.

© 2022 The Authors. Advanced Functional Materials published by Wiley-VCH GmbH

16163028, 2022, 37, Downloaded from https://onlinelibrary.wiley.com/doi/10.1002/adfm.202201881 by Universita Degli Studi Di Roma, Wiley Online Library on [25/01/2023]. See the Terms and Conditions (https://onlinelibrary.wiley.com/terms-and-conditions) on Wiley Online Library for rules of use; OA articles are governed by the applicable Creative Commons License